Materials Research Bulletin 97 (2018) 150–157

Contents lists available at ScienceDirect

Materials Research Bulletin

journal homepage: www.elsevier.com/locate/matresbu

Heterogeneous photocatalytic Cr(VI) reduction with short and long nanotubular TiO_2 coatings prepared by anodic oxidation

María L. Vera[a,b,c], Hernán D. Traid[a,b,c], Edgard R. Henrikson[a,c], Alicia E. Ares[a,b,c], Marta I. Litter[b,d,e,*]

[a] Instituto de Materiales de Misiones, IMAM (CONICET-UNaM), Félix de Azara 1552, 3300 Posadas, Misiones, Argentina
[b] Consejo Nacional de Investigaciones Científicas y Técnicas, Godoy Cruz 2290, 1425 Buenos Aires, Argentina
[c] Facultad de Ciencias Exactas, Químicas y Naturales, Universidad Nacional de Misiones, Félix de Azara 1552, 3300 Posadas, Misiones, Argentina
[d] Gerencia Química, Centro Atómico Constituyentes, Comisión Nacional de Energía Atómica, Av. Gral. Paz 1499, 1650 San Martín, Prov. de Buenos Aires, Argentina
[e] Instituto de Investigación e Ingeniería Ambiental, Universidad Nacional de Gral. San Martín, Campus Miguelete, Av. 25 de Mayo y Francia, 1650 San Martín, Prov. de Buenos Aires, Argentina

ARTICLE INFO

Article history:
Received 5 January 2017
Received in revised form 4 August 2017
Accepted 8 August 2017
Available online 26 August 2017

Keywords:
TiO_2 nanotubes
Anodic oxidation
Hexavalent chromium
Heterogeneous photocatalysis

ABSTRACT

Nanotubular TiO_2 coatings prepared by anodic oxidation of titanium were evaluated for the first time in the photocatalytic Cr(VI) reduction in the presence of EDTA. Small nanotubes (SN) were prepared by using aqueous hydrofluoric acid as electrolyte, and long nanotubes (LN) were made by using an ethylene glycol solution containing ammonium fluoride and water. The samples were characterized by scanning electron microscopy, X-ray diffraction and UV–Vis diffuse reflectance spectroscopy. The photocatalytic reactions were performed using $[Cr(VI)]_0 = 0.8$ mM, an EDTA/Cr(VI) molar ratio = 1.25 and pH 2. The photocatalytic activity increased with the applied voltage due to an increase of the average diameter, wall thickness and length of the nanotubes. The most active SN coating yielded 98% of Cr(VI) transformation after 300 min, while all LN samples achieved a complete transformation in the same time or less. The photocatalytic activity was in almost cases higher than that of a P25 supported sample.

1. Introduction

TiO_2 is a well-known photocatalyst for water and air disinfection and decontamination. When TiO_2 is irradiated under UV light, very reactive species are created, able to transform pollutants by heterogeneous photocatalysis (HP) [1]. Although photocatalysis has been widely used with TiO_2 suspensions, the recovery of the catalyst involves expensive and time-consuming separation processes, which could be avoided by the immobilization of the photocatalyst on suitable substrates [2]. However, immobilization generally leads to a decrease of the overall photocatalytic activity due to a reduction of the surface area and limitations in mass transfer. To solve these problems, the use of one-dimensional nanostructures such as nanotubes has been recently proposed. TiO_2 nanotubes combine unique geometrical features (high surface/volume ratio and short diffusion path) with remarkable optical, electrical and chemical properties such as faster electron transport and lower charge recombination [3,4]. This explains the great variety of use of these materials in advanced applications, such as sensors, dye sensitized solar cells, hydrogen generation, molecular filtration and drug delivery ([5] and references therein) including water and air decontamination [6]. One of the major challenges for the application is to obtain TiO_2 coatings with high surface area and photocatalytic activity, combined with good mechanical strength to allow reuse [7].

TiO_2 nanotubes have been produced by a number of methods, e.g., use of templates of nanoporous alumina, sol–gel transcription processes with organo-gelator templates, seeded growth mechanisms, and hydrothermal techniques (see e.g., [8]). None of these methods, however, offers a superior control over the nanotube dimensions compared with titanium anodization [9], especially in a fluoride-based electrolyte [5,10,11]. As very well known, anodic oxidation is a simple and low-cost process that creates an oxide coating over a metallic surface, whose properties depend on the electrolyte composition and the electrochemical parameters [5]. When the electrolyte contains fluoride ions (F^-), typical morphologies of titania nanotubes are obtained depending on the

* Corresponding author at: Gerencia Química, Centro Atómico Constituyentes, Comisión Nacional de Energía Atómica, Av. Gral. Paz 1499, 1650 San Martín, Buenos Aires, Argentina Tel.: +54 11 6772 7016; fax: +54 11 6772 7886.
E-mail addresses: marta.litter@gmail.com, litter@cnea.gov.ar (M.I. Litter).

http://dx.doi.org/10.1016/j.materresbull.2017.08.013
0025-5408/

competition between TiO_2 formation and chemical dissolution of the anodic titania layer [12–16] (see the supporting information (SI, Section S1) for a description of the process). The electrolyte composition determines the production of different types of nanotubes: a 1st generation prepared in aqueous HF, with lengths up to 500 nm; a 2nd generation up to 5 μm long, grown in aqueous solutions of fluoride salts; a 3rd generation of smoother and longer nanotubes, up to 100–1000 μm, grown in organic electrolytes containing F^- and small amounts of water (0.1–5 wt%) ([17] and references therein). To assess the photocatalytic activity of anodic nanotubes, some works analyzed the removal of uranium(VI) and lead(II) [18], Paraquat [19] or phenol [20,21], but most of them used the degradation of dyes [22–29]. However, degradation of dyes is not a suitable test because parallel processes, such as photolysis, reductive bleaching or sensitization, interfere with the photocatalytic process [10,30–32], making unclear the true phenomenon. For this reason, the use of other well established probe systems, such as the very good and fast Cr(VI) conversion to Cr(III) in the presence of ethylenediaminetetraacetic acid (EDTA, see e.g. references [33–43]), is highly desirable for a better comparison of the photocatalytic activities, through a very simple monitoring of the Cr(VI) concentration. In addition, this represents a good alternative for the removal of dangerous hexavalent chromium species from aqueous systems. Cr(III) has been observed in TiO_2 coatings as a product of the Cr(VI) photocatalytic transformation [44,45]. Although many works have been done for TiO_2 photocatalytic Cr(VI) reduction, either in suspension or supported, none of them have been done with anodic TiO_2 nanotubes.

In the present work, the activity of two types of nanotubular TiO_2 coatings synthesized by anodic oxidation of titanium has been tested for the first time with the Cr(VI)/EDTA system. 1st generation small nanotubes (SN) were made by using aqueous hydrofluoric acid as electrolyte, and 3rd generation long nanotubes (LN) were prepared by using an organic solution of ethylene glycol (EG) containing ammonium fluoride and water. The influence of the applied voltages on the photocatalytic activity has been evaluated.

2. Experimental

2.1. Materials and methods

All chemicals were reagent grade and used without further purification. Hydrofluoric acid (HF, Cicarelli, 48%), ammonium fluoride (NH_4F, Biopack), EG (Biopack, 99%), potassium dichromate ($K_2Cr_2O_7$, Merck), EDTA (Riedel de Haën AG, Seeelze – Hannover), diphenylcarbazide (DFC, UCB), acetone (Anedra, 99.5%) and phosphoric acid (Biopack, 85%) were used. All other reagents were of the highest available purity. Deionized water (conductivity = 0.05–0.06 $\mu S\,cm^{-1}$) was obtained with an OSMOION Agua Ultrapura Apema equipment. All pH adjustments were made with perchloric acid (Merck, 70–72%). P25 Evonik was used as received. A PHM210 Meter Lab® (Radiometer Analytical) pHmeter was used. For anodization, a JMB direct current source, model LPS360DD, was used. For dip-coating, a homemade dip-coater was employed. For the thermal treatments, a SIMCIC oven was employed. A Hewlett-Packard diode array UV–Vis spectrophotometer model HP 8453 A was used for spectrophotometric measurements.

Scanning electron microscopy (SEM) was performed using a Carl Zeiss Supra 40 equipment with an Oxford Instruments INCA x-act detector for energy dispersive X-ray spectroscopy (EDS). The analysis of the SEM images was made with the ImageJ software [46]; the average inner diameter (D_i) and the wall thickness (W) of the nanotubes were determined as the average of 50 measurements of the top view SEM micrographs, and the lengths (L) were measured after scratching the coatings to obtain cross-sectional views. For glancing incidence X-ray diffraction (GI-XRD), a Panalytical, Empyrean diffractometer with a Pixel 3D detector was used with CuK_α radiation at a scan rate of 0.02° (2θ)/s and a glancing angle of 1°. The accelerating voltage and the applied current were 40 kV and 30 mA, respectively. The–UV-Vis diffuse reflectance spectra (DRS) of the samples were obtained at room temperature in air using a Shimadzu, UV-3600 UV–Vis–NIR spectrophotometer equipped with an integrating sphere and $BaSO_4$ as the reference.

2.2. Photocatalyst preparation

Commercially pure titanium plates (Grade 2 according to ASTM B367), 30 × 20 mm^2 and 2 mm thick were used as substrates for the coatings. They were polished with abrasive SiC papers (Köln) with decreasing granulometry (from # 120 up to # 1500), finishing with diamond paste (Praxis, 1 μm) lubricated with EG. For polishing, a mechanical polishing machine (250 rpm) was used. The prepared surfaces were then cleaned with water and detergent, rinsed with alcohol and hot air dried. One of the substrates (labeled as Ti) was not anodized. To protect the anodic contact, an acrylic protection was used in the longest side of the plate, giving ~9 cm^2 of effectively anodized surface (see Fig. S1(a)). The uncoated section was cut previously to the irradiation.

Anodic oxidation was carried out at room temperature (25 °C) in a plastic beaker containing the electrolyte solution. A DC electric current was applied at a constant voltage between two Pt sheets used as cathodes and a Ti anode, separated each other by 5 cm, as illustrated in Fig. S1(b); the evolution of the cell voltage (V) and the current density (J) were followed during the process (Fig. S2). Immediately after the oxidation, the samples were rinsed with demineralized water and dried with hot air. Some samples were submitted to thermal treatments (TT) in the oven at 450 °C in air at a 10 °C min^{-1} heating rate, and the cooling down was made inside the oven.

Short nanotubes (SN) were obtained in 1% v/v HF at 8, 12, 15 and 20 V applied voltages during 15 min, followed by a TT lasting 1 h. Long nanotubes (LN) were obtained in an EG-based solution containing 0.6 wt% of NH_4F and 3.5 wt% of water with applied voltages of 20, 30, 40, 50 and 60 V during 2 h. The TT lasted 2 h. The complete nomenclature for the coated plates were SN or LN for short or long nanotubes, respectively, followed with the letter V and the voltage value, e.g. SN-V8, LN-V50, etc. The suffixes TTS and TTL were added to identify the TT applied to short or long nanotubes, respectively.

A sample of supported P25 prepared as described in Kleiman et al. [38] was used as reference in the photocatalytic tests.

2.3. Photocatalytic tests

A 0.4 mM $K_2Cr_2O_7$ aqueous solution containing 1 mM EDTA as sacrificial synergetic agent was used for the photocatalytic tests. The initial pH was adjusted to 2. The photocatalyst samples were immersed into 10 mL of this solution contained in cylindrical reactors (3.6 cm diameter and 5 cm high) under magnetic stirring, and six samples were irradiated simultaneously using a BLV MHL-404 UV lamp ($\lambda > 250$ nm, maximum emission at 365 nm). Between the UV lamp and the reactor, a water filter and a glass filter were located, to avoid IR radiation and UV wavelengths lower than 300 nm, respectively. The mean UV irradiance incident on the surface of the solution (E^0) was 2700 $\mu W\,cm^{-2}$, measured at 365 nm with a Spectroline DM-365 XA radiometer.

Prior to irradiation, the solutions were kept under stirring in the dark for 30 min, to assure the adsorption equilibrium between the pollutant and the photocatalyst. No significant changes in Cr(VI)

concentration were observed after this dark period. 50 μL samples were taken each hour and diluted in 3 mL of water for analysis. Changes in Cr(VI) concentration were spectrophotometrically monitored through the DFC method at 540 nm [47] using a Hewlett-Packard diode array UV–Vis spectrophotometer, model HP 8453 A. To evaluate the homogeneous photochemical reduction of Cr(VI), the model pollutant was irradiated in the absence of TiO_2 (blank experiment). An error of 5% was assumed for the photocatalytic experiments. The fitting of the experimental points was made with Origin 8.0 software, with reduced c^2 as the iteration-ending criterion.

3. Results and discussion

3.1. Synthesis of coatings

In Section S3 of SI, the evolution of current density during the early stages of anodization to obtain SN and LN samples is described, indicating the different stages leading to the corresponding samples.

3.2. Characterization of the coatings

Samples have been characterized by SEM/EDS, DRS and XRD.

3.2.1. SEM images: morphology

In Fig. 1, top view micrographs of the SN samples are presented. Fig. 1(a) and (b) shows that the substrates anodized at 8 and 12 V, respectively, exhibit a sponge-like structure with the presence of randomly dispersed pores, a morphology that commonly appears prior to the formation of the nanotubes [48]. The sample obtained at a higher voltage (15 V, Fig. 1(c)) clearly evidences the top view of a nanotubular structure, with defined walls in light gray. At 20 V, the same nanotube structure, although with a larger diameter, is visibly observed (Fig. 1(d), see a cross section of about 200 nm length in the inset). This indicates the significant influence of the voltage on the formation of the nanotubes [14].

In Fig. 2, top view micrographs of the LN samples are presented, where, except in Fig. 2(a), another nanostructure identified as 'nanograss' [49] is observed, being a remnant of the oxides formed at the early anodization stages due to the limited dissolution in organic solutions [17,50]. The inset in Fig. 2(e) shows the cross-sectional view of the corresponding coating. Although different strategies for preventing the formation and removal of the nanograss were developed [51–53], in photocatalytic applications it could be important to maintain those nanostructures because they increase the total surface area of the catalyst, as we will see later.

In Fig. S3, the closed bottom of the nanotubes are observed, showing ribs along the walls; in fact, smooth nanotube walls have been reported when the water content in organic electrolytes did not exceed 0.5 wt% [16]. However, as in this work the water content of the EG solution was 3.5 wt%, the ribs may be the result of oxygen evolution due to the anodic electrolysis of water [16,52]. It is important to mention that when voltages higher than 50 V were applied in our experiments of LN formation, detachment of the coatings began to be observed.

In Fig. S4, a correlation between the mean values of *Di*, *W* and *L* of SN and LN with the applied voltage is presented. The influence of the electrolyte on the dimensions of the nanotubes can be observed comparing samples obtained at 20 V (SN-V20-TTS and LN-V20-TTL). Whilst the electrolyte seems to have no influence on *W*, larger D_i and smaller *L* are obtained in the aqueous electrolyte. Regarding *L*, in both cases, an exponential growth with the voltage

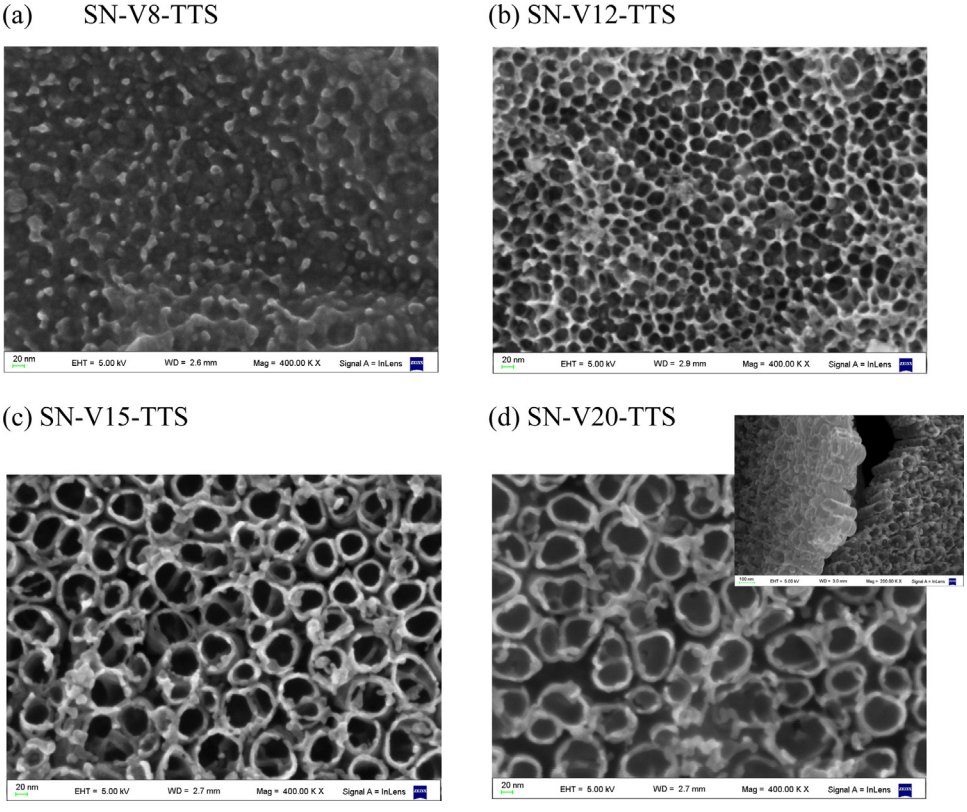

Fig. 1. SEM micrographs of the top of the SN coatings obtained at different voltages. Inset in (d): cross-sectional view of the corresponding coating.

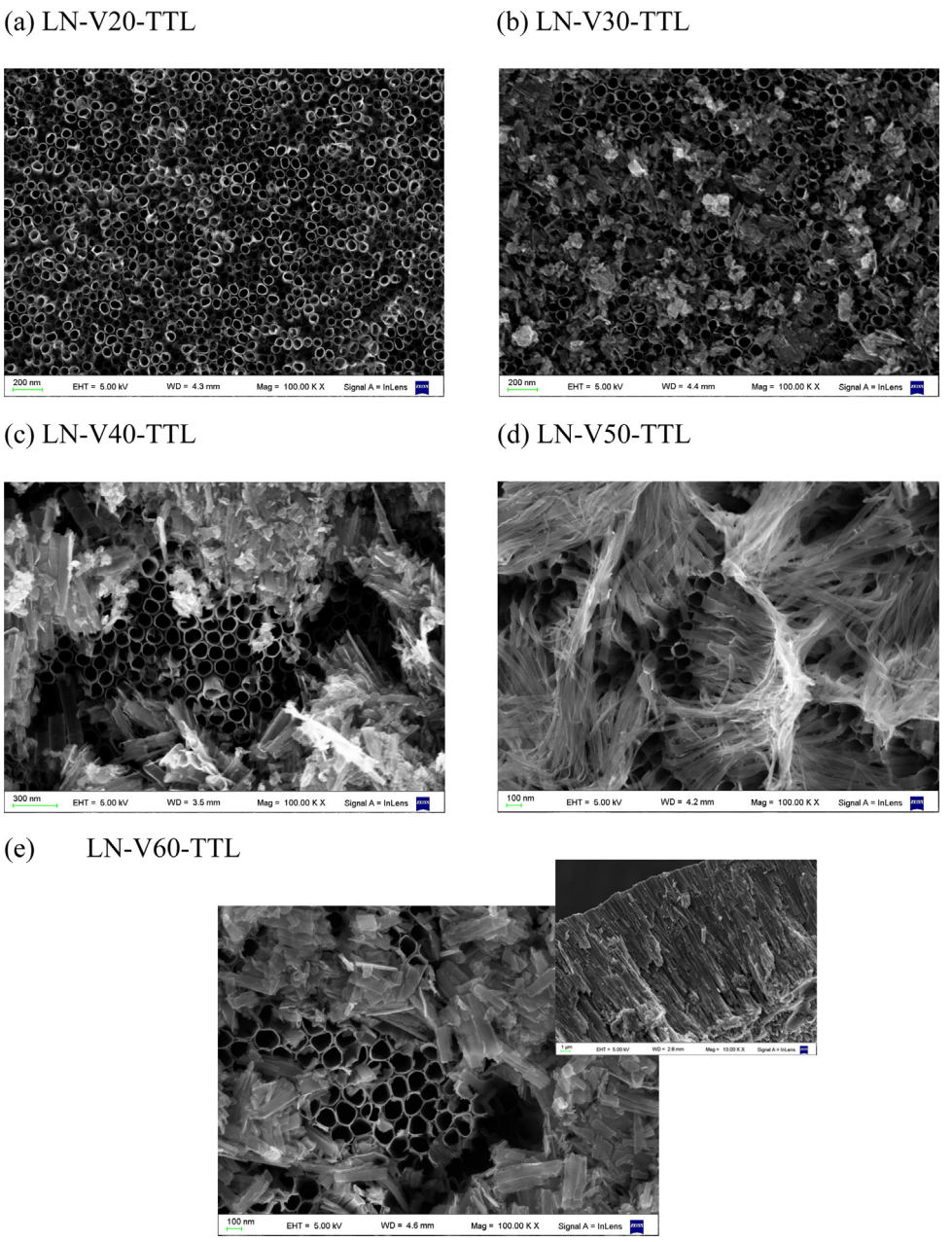

Fig. 2. SEM micrographs of the top of the LN coatings obtained at different voltages. Inset in (e): cross-sectional view of the corresponding coating.

is observed (Fig. S4). For SN, the time required to form the nanotubes is about 6 min; further increase of the anodization time results in more uniform nanotubes but without changes in *L*, because the oxidation/dissolution equilibrium has been reached [52], and the relatively high dissolution rate in the aqueous electrolyte allows limited lengths not exceeding 500 nm [14]. In contrast, LN samples show a relatively faster growth rate in the first 30 min of anodization due to the relatively lower dissolution rate, and with a slightly retarded growth rate due to the limit of ion diffusion in the thicker layer [5]. *L* of LN were between 1 and 15 μm, in agreement with literature data ([17] and references therein).

An elemental analysis of the coatings was performed using EDS as a preliminary evidence of the presence of TiO_2. In Fig. S5, EDS spectra of SN and LN samples are presented and the characteristic peaks have been associated with Ti and O. In the case of LN-V40-TL (Fig. S5(b)), the quantitative analysis reveals that the atomic ratio of Ti and O is close to 1:2, indicating that TiO_2 is the structure of the deposited materials. In contrast, a quantitative analysis could not be possible for SN-V20-TS (Fig. S5(a)), because the SN coatings have a thickness of 200 nm, while the EDS penetration is around 1 μm; therefore, the adsorbed quantities in the 200 nm superficial layer could represent less than the detection limit of EDS (0.1% w) (Table of Fig. S5(b)).

Table 1 shows the results of D_i, *W*and *L* for all new samples, extracted from the SEM images, together with the calculated bandgaps discussed later in Section 3.2.2. As expected, increasing applied voltages resulted in higher dimensions of SN and LN because a higher voltage increases both the growth rate of the nanotube arrays and the current density, disturbing the chemical dissolution and leading to longer TiO_2 nanotubes of larger diameter [14,17].

Table 1
Characteristic dimensions and calculated bandgaps of SN and LN samples.

Sample	V (V)	D_i (nm)	W (nm)	L (**)	E_g (eV)
SN-V8-TTS	8	–*	–*	34 ± 17	–*
SN-V12-TTS	12	27 ± 12	5 ± 4	37 ± 18***	3.31
SN-V15-TTS	15	50 ± 23	8 ± 4	40 ± 20	3.55
SN-V20-TTS	20	63 ± 25	12 ± 7	200 ± 58	3.39
LN-V20-TTL	20	40 ± 16	14 ± 4	1 ± 0.5	3.23
LN-V30-TTL	30	60 ± 18	15 ± 4	2 ± 1***	3.20
LN-V40-TTL	40	82 ± 21	15 ± 8	3 ± 1	3.18
LN-V50-TTL	50	93 ± 14	20 ± 1	8 ± 1	3.20
LN-V60-TTL	60	97 ± 17	21 ± 5	15 ± 3	3.14

* Not measured.
** SN samples in nm and LN samples in μm.
*** estimated by interpolation from Fig. S4.

3.2.2. Diffuse reflectance spectra: bandgaps

The diffuse reflectance spectra (Fig. 3) were used to calculate the bandgaps of selected samples through Tauc plots (E_g was obtained by extrapolating to zero a linear fit to a plot of $(khv)^{1/2}$ against hv, as reported in reference [54]); the values are listed in Table 1.

The bandgap estimated from DRS measurements for SN samples is ~3.4 eV. This value, higher than those reported for bulk anatase and rutile (3.2 and 3.0 eV, respectively [5]), is probably a result of the influence of the substrate specular reflection (shown in the inset of Fig. 3(a)) on the spectra of the samples because of the low coating thickness (< 1 μm Table 1) [19,55]. In the case of thin coatings, the light is not fully absorbed, and part of it is reflected at the coating-substrate interface; therefore, the overlapping with the Ti spectra produces a blue shift of the maximum diffuse reflectance and, consequently, on the bandgap value. Moreover, a blue shift might be due to a quantum size effect and interband transitions in SN samples (wall thicknesses ≤12 nm) [56]. In contrast, LN coating thicknesses are well above 1 μm, and wall thicknesses are higher than 12 nm (Table 1), making negligible the influence of the substrate and the quantum confinement. Thus, the bandgap values of these samples are around 3.2 eV, in agreement with the anatase content (see Section 3.2.3).

3.2.3. XRD patterns: crystalline structures

Fig. 4 shows the XRD patterns of the Ti substrate and the coatings. In the spectra of SN-V20 and LN-V60, only diffraction peaks of the Ti substrate can be seen, indicating that the nanotubes without TT are amorphous.

Fig. 4(a) shows, for coatings obtained at 8 and 20 V, that the TT allows crystallization into anatase (A) and rutile (R). According to the literature, A is formed in the nanotube walls, while R grew from the Ti metal by thermal oxidation [5,57]; the physical constraints imposed by the size of the nanotube walls make difficult the A to R transformation [5,58]. The A fraction of selected samples was calculated using the equation: $X_A = 1/[1 + 2.18\ (I_R/I_A)] \pm 2\%$, where X_A is the molar fraction of A, and I_A and I_R are the total areas of the peaks of the X-ray intensities of the A and R strongest peaks, (1 0 1) at $2\theta = 25.28°$ and (1 1 0) at $2\theta = 27.46°$, respectively [59]. It could be observed that the A/R ratio increases with the increase in anodization voltages; e.g., the SN-V20-TTS coating presents a higher A content (54% anatase; 1.17 ratio) compared with SN-V8-TTS (14% anatase; 0.16 ratio). This is easily explained considering that the higher voltage produces larger nanotubes and more A is formed in the walls, while the R content does not change because the thermal treatment was the same. Fig. 4(b) shows that, after the TT, LN samples are composed only of anatase [19,27]. It has been reported that A nanocrystals with a size below a critical value (~45 nm [60]) present a lower total (bulk and surface) free energy [61] and are more stable than R crystals. In this case, while the oxide layer underlying the nanotube array could remain as rutile [57], this phase is not seen in the XRD spectra due to the great length of tubes obtained in the organic electrolyte [5,57].

3.3. Cr(VI)/EDTA photocatalytic experiments

The photocatalytic activities of SN and LN coatings were tested with the Cr(VI)/EDTA system ($[Cr(VI)]_0 = 0.8$ mM; [EDTA]/[Cr(VI)] = 1.25; pH 2; $E^0 = 2700\ \mu W\ cm^{-2}$). Fig. 5 presents the results of normalized Cr(VI) removal using the new coatings together with those obtained over a P25 sample containing 0.03 mg TiO_2 cm^{-2} [38], and that obtained in the absence of photocatalyst under similar conditions (blank). It can be seen that the photocatalytic Cr (VI) reduction with all the new coatings is faster than the reduction in the absence of TiO_2, and all samples (except SN-V8-TTS) exhibit a higher photocatalytic activity than the P25 sample. It is important to remark that the amount of TiO_2 present in the anodic coatings is not known and is not easy to be estimated. Although the preparation and characteristics (e.g., thickness and amount of TiO_2) of this P25 sample are different from those of the anodic ones [10], a reasonable and useful comparison of the reactivity can be extracted.

With respect to the morphological and structural stability of the nanotubular coatings, it is important to mention that short and long nanotubes kept their shape and structure after the photocatalytic tests, without collapsing evidence.

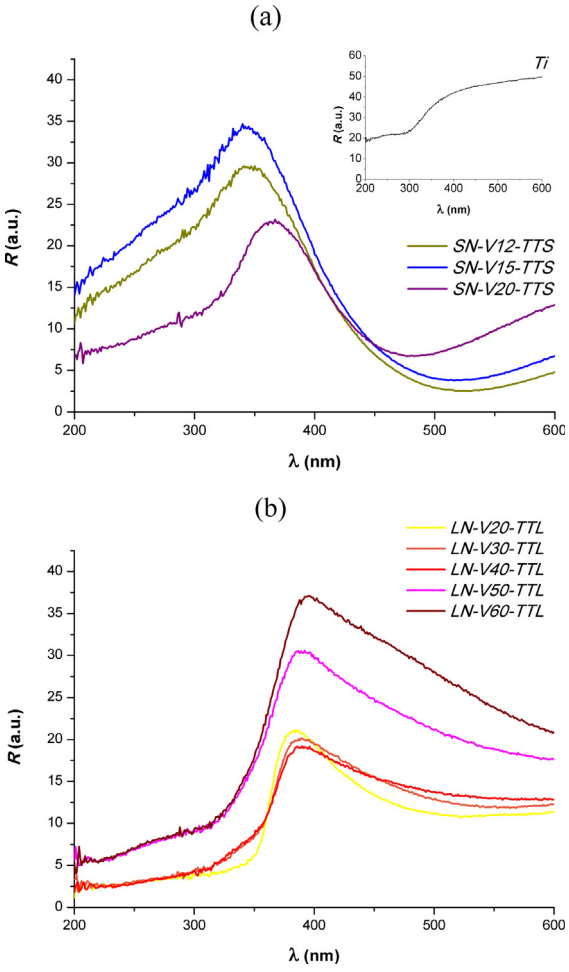

Fig. 3. UV–Vis diffuse reflectance spectra of selected samples: (a) SN and (b) LN.

The experimental points for the homogeneous reaction could be fitted with Eq. (1):

$$\frac{C}{C_0} = e^{-k_1 t} \quad (1)$$

where C is the Cr(VI) concentration in solution, C_0 is the Cr(VI) concentration at the beginning of the photocatalytic test, and k_1 is the pseudo-first order kinetic constant. The k_1 value, 2.77×10^{-3} min^{-1} ($R^2 = 0.992$), was obtained for the blank and is similar to those previously reported for the same system under similar conditions [38–40]. For the reaction with supported photocatalysts, we used the model previously reported by us, in which the experimental points are adjusted with an equation composed of a first order term corresponding to the homogeneous reaction (k_1) plus a zero order term describing the reaction on the immobilized catalyst surface (k_0). This model considers that the area of the photocatalyst is saturated by Cr(VI) adsorbed during the photocatalytic run, making the reduction rate independent of the Cr(VI) concentration in solution [38–40]:

$$\frac{C}{C_0} = \left(1 + \frac{k_0}{k_1}\right) e^{-k_1 t} - \frac{k_0}{k_1} \quad (2)$$

k_1 was calculated by Eq. (1) and used to adjust the curves of the immobilized catalysts to obtain the k_0 values. For SN samples, the rate constants calculated from the plots are presented in Table 2, together with the extent of Cr(VI) removal after 300 min irradiation. The fitting curves using Eq. (2) show a good agreement ($R^2 > 0.97$) with the experimental points.

As shown in Fig. 5(a) and Table 2, the maximum removal (98%) obtained for SN samples occurred with SN-V20-TTS, the percentages of removal and the k_0 values increasing with the applied voltage. This enhancement of the photocatalytic Cr(VI) reduction can be explained because of the higher diameters and lengths of the samples (Table 1), which allows the pollutant and the light to penetrate deeper in the tubes [19]. The relationship between higher anodization voltages and higher activities for TiO_2 anodic nanotubes has been also reported for methyl orange degradation [26,62]. The lowest removal (67%) was obtained with SN-V20, indicating the importance of the crystallinity of the photocatalyst for the activity [13]. Similar k_0 values for Cr(VI) transformation were reported for porous (non nanotubular) TiO_2 coatings made by cathodic arc [38], anodic spark oxidation [40], and sol–gel dip-coating combined with P25 [39].

In the case of LN coatings, a complete Cr(VI) removal occurred at 300 min for all samples. Moreover, the complete removal was faster for LN-V50-TTL and LN-V60-TTL than for LN-V20-TTL, LN-V30-TTL and LN-V40-TTL (3 h and 4 h, respectively). With the sample without TT (LN-V60), the reaction was even slower, the

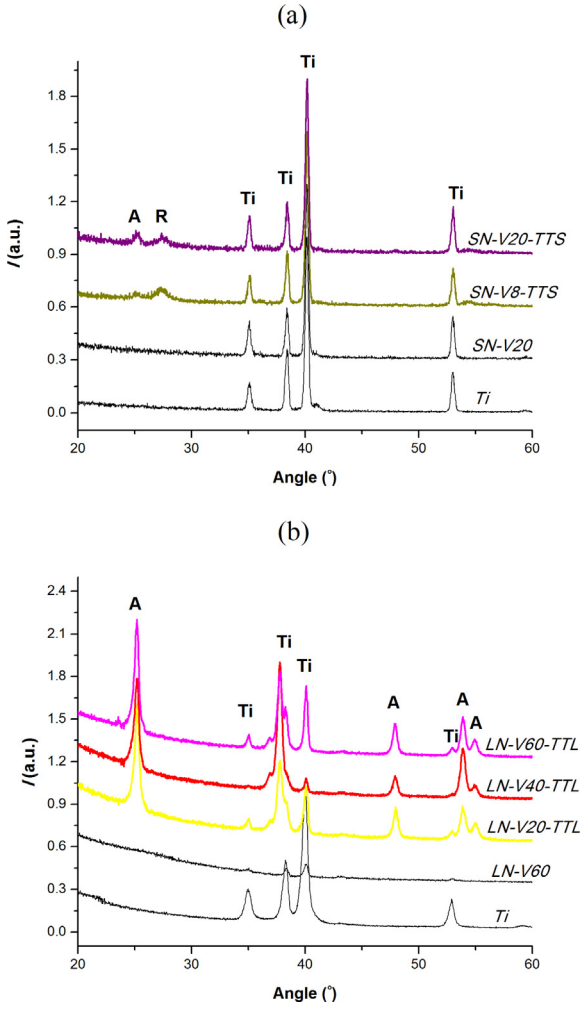

Fig. 4. XRD patterns of: (a) SN and (b) LN. Ti = titanium, A = anatase, R = rutile.

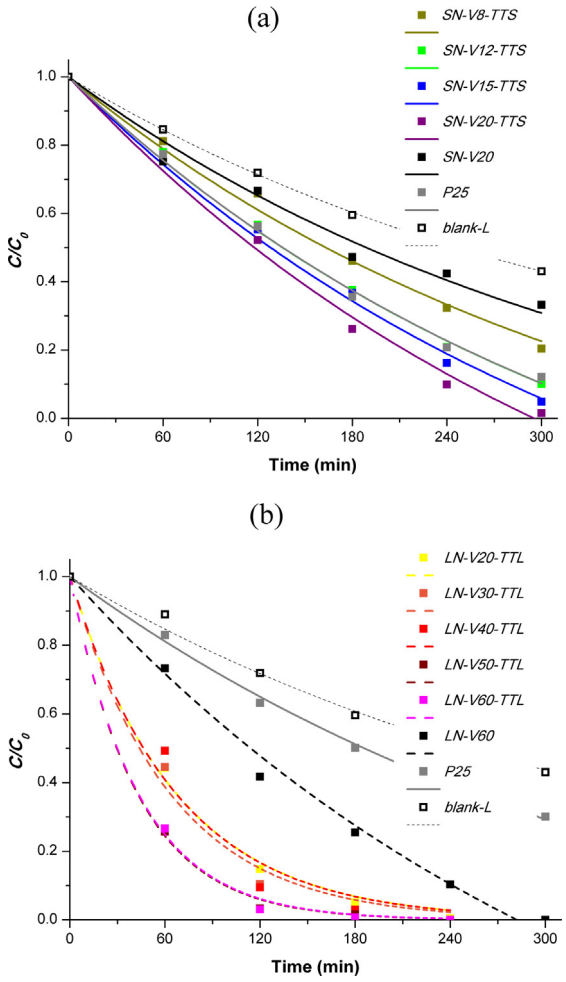

Fig. 5. Temporal evolution of normalized Cr(VI) concentration in photocatalytic experiments of Cr(VI) transformation in the presence of EDTA under UV irradiation over: (a) SN; (b) LN. Conditions: $[Cr(VI)]_0 = 0.8$ mM; [EDTA]/[Cr(VI)] = 1.25; pH 2; $E^0 = 2700\ \mu W\ cm^{-2}$. The dashed lines are the fittings of the experimental points with Eq. (1), and the solid lines are the fittings with Eq. (2). The adjusted curve of LN-V60-TTL is superimposed to the adjusted curve of LN-V50-TTL.

Table 2
Zero order kinetic constant (k_0) and percentage of Cr(VI) removal in the presence of EDTA at 300 min for SN samples extracted from Fig. 5(a).

Sample	$k_0 \times 10^3$ (min^{-1})	R^2	% Cr(VI) removal
Blank	2.77*	0.992	57
SN-V8-TTS	1.03	0.993	80
SN-V12-TTS	1.64	0.998	90
SN-V15-TTS	1.86	0.997	95
SN-V20-TTS	2.19	0.993	98
SN-V20	0.63	0.977	67
P25	1.64	0.997	88

* k_1 (2.77×10^{-3} min^{-1}).

Table 3
First order kinetic constants (k_1) and time for the complete Cr(VI) removal in the presence of EDTA for LN samples, extracted from Fig. 5(b).

Sample	$k_1 \times 10^2$ (min^{-1})	R^2	100% Cr(VI) (min) removal
Blank	0.277	0.992	>300
LN-V20-TTL	1.488	0.997	240
LN-V30-TTL	1.581	0.989	240
LN-V40-TTL	1.494	0.980	240
LN-V50-TTL	2.347	0.999	240
LN-V60-TTL	2.319	0.998	180
LN-V60	0.769	0.968	300
P25	0.790	0.998	>300

complete transformation occurring after 5 h of irradiation, reinforcing the importance of the crystallinity of the photocatalyst [13]. Once again, the higher the voltage, the faster the photocatalytic Cr(VI) reduction, indicating that the removal depends on the accessibility of light and contaminant to the nanotubes, given by the higher diameters; the content of TiO_2, given by the higher wall thickness and length of the nanotubes (Table 1), is also a relevant factor. In this case, all curves responded to a first order rate law (Eq. (1)), as shown in dashed lines of Fig. 5(b). The calculated k_1 rate constants are presented in Table 3, together with the time for the complete Cr(VI) removal.

In order to evaluate the purity of the coatings after the photocatalytic tests, EDS spectra of LN-V40-TTL after the test were taken (Fig. S6). Ti, O, C and Cr were detected. Ti and O correspond to the TiO_2 coating, C comes from the remaining EDTA used as organic electron donor and Cr comes from the Cr(III) adsorbed on the coatings after the Cr(VI) photocatalytic transformation [44,45]. The mapping of each element shows a homogeneous distribution of all the elements on the surface. In the EDS of SN-V20-TTS after the photocatalytic test, only Ti and O were detected. This is a logical result taking into account that the SN coatings have a thickness of 200 nm while the EDS penetration is around 1 μm; therefore, the adsorbed quantities in the 200 nm superficial layer could represent less than the detection limit of EDS (0.1% w).

The top nanograss in some LN coatings (Fig. 2) was not detrimental for the photocatalytic activity. This was in contrast with that reported by Mazzarolo et al. [63] on AO7 dye photocatalytic experiments, where the observed decrease on the activity was attributed to the nanograss hindering the access of reactants to the tubes. In the present case, probably a compromise between crystalline TiO_2 mass and surface area can explain the enhanced photocatalytic rate.

The different kinetic regime obeyed by the SN and LN coatings can be attributed to the higher surface areas of the long nanotubes that cannot be saturated by adsorbed chromium (see Fig. S6), making, in this case, the reduction rate dependent on the Cr(VI) concentration in solution, as the case of the homogeneous systems.

4. Conclusions

Short (SN) and long nanotubes (LN), prepared by anodic oxidation of commercially pure titanium in aqueous HF and EG based F^- solutions as electrolytes, presented high photocatalytic activity for Cr(VI) reduction in the presence of EDTA due to their high surface area and crystalline structure. The reaction over SN samples followed a combined rate law (first order plus cero order), and a pseudo-first order rate represented better the experimental results for LN coatings. The photocatalytic activity of the nanotubes for Cr(VI) reduction increased with the applied voltage, as this caused an increase of the average diameter, wall thickness and length, and was, in almost cases (except SN-V8-TTS), higher than that of a supported P25 sample.

The application of these materials as immobilized TiO_2 heterogeneous photocatalysts for water and air decontamination can be foreseen, especially for those obtained in aqueous HF solution at 20 V and those obtained in EG-based solution at voltages below 50 V, in both cases with subsequent TT.

Acknowledgments

This work was supported by CONICET and Agencia Nacional de Promoción Científica y Tecnológica (ANPCyT) from Argentina under PICT-2011-0463, PICT-2011-1378 and PICT-2012-2952 grants. The authors thank Daniel Vega from the DRX Laboratory, Department of Condensed Matter Physics (CAC-CNEA) and to Enrique San Román from INQUIMAE-UBA for the DRS. Edgard Henrikson thanks Consejo Interuniversitario Nacional (CIN) of Argentina for a fellowship.

Appendix A. Supplementary data

Supplementary data associated with this article can be found, in the online version, at http://dx.doi.org/10.1016/j.materresbull.2017.08.013.

References

[1] U. Riaz, S.M. Ashraf, J. Kashyap, Mater. Res. Bull. 71 (2015) 75–90.
[2] D. Robert, V. Keller, N. Keller, Immobilization of a semiconductor photocatalyst on solid supports: methods, materials, and applications, in: P. Pichat (Ed.), Photocatalysis and Water Purification. From Fundamentals to Recent Applications, Wiley-VCH, Weinheim, 2013, pp. 145–178.
[3] Y.L. Pang, S. Lim, H.C. Ong, W.T. Chong, Appl. Catal. A 481 (2014) 127–142.
[4] S.P. Albu, A. Ghicov, S. Aldabergenova, P. Drechsel, D. Le Clere, G.E. Thompson, J. M. Macak, P. Schmuki, Adv. Mater. 20 (2008) 4135–4139.
[5] C.A. Grimes, G.K. Mor, TiO_2 Nanotubes Arrays, Synthesis, Properties and Applications, Springer, New York, 2009.
[6] S.-Y. Lee, S.-J. Park, J. Ind. Eng. Chem. 19 (2013) 1761–1769.
[7] K. Nakata, A. Fujishima, J. Photochem. Photobiol. C 13 (2012) 169–189.
[8] M. Stodolny, R. Zagrodnik, G. Nowaczyk, S. Jurga, Mater. Res. Bull. 94 (2017) 335–341.
[9] A.-Z. Liao, C.-W. Wang, J.-B. Chen, X.-Q. Zhang, Y. Li, J. Wang, Mater. Res. Bull. 70 (2015) 988–994.
[10] P. Pichat, Molecules 19 (2014) 15075–15087.
[11] E. Zalnezhad, E. Maleki, S.M. Banihashemian, J.W. Park, Y.B. Kim, M. Sarraf, A.A. D.M. Sarhan, S. Ramesh, Mater. Res. Bull. 78 (2016) 179–185.
[12] D. Gong, C.A. Grimes, O.K. Varghese, W. Hu, R.S. Singh, Z. Chen, E.C. Dickey, J. Mater. Res. 16 (12) (2001) 3331–3334.
[13] I. Paramasivam, H. Jha, N. Liu, P. Schmuki, Small 8 (20) (2012) 3073–3103.
[14] H.-J. Oh, I.-K. Kim, K.-W. Jang, J.-H. Lee, S. Lee, C.-S. Chi, Met. Mater. Int. 18 (4) (2012) 673–677.
[15] A. Jaroenworaluck, D. Regonini, C.R. Bowen, R. Stevens, D. Allsopp, J. Mater. Sci. 42 (2007) 6729–6734.
[16] K.S. Raja, T. Gandhi, M. Misra, Electrochem. Commun. 9 (2007) 1069–1076.
[17] D. Regonini, C.R. Bowen, A. Jaroenworaluck, R. Stevens, Mater. Sci. Eng. R 74 (12) (2013) 377–406.
[18] M. Bonato, K.V. Ragnarsdottir, G.C. Allen, Water Air Soil Pollut. 223 (7) (2012) 3845–3857.
[19] C.B.D. Marien, T. Cottineau, D. Robert, P. Drogui, Appl. Catal., B: Environ. 194 (2016) 1–6.
[20] Z. Hua, Z. Dai, X. Bai, Z. Ye, H. Gu, X. Huang, J. Hazard. Mater. 293 (2015) 112–121.

[21] P. Mazierski, M. Nischk, M. Golkowska, W. Lisowski, M. Gazda, M. Winiarski, T. Klimczuk, A. Zaleska-Medynska, Appl. Catal., B: Environ. 196 (2016) 77–88.
[22] H.-J. Oh, J.-H. Lee, Y.-J. Kim, S.-J. Suh, J.-H. Lee, C.-S. Chi, Appl. Catal., B: Environ. 84 (2008) 142–147.
[23] M. Erol, T. Dikici, M. Toparli, E. Celik, J. Alloys Compd. 604 (2014) 66–72.
[24] C.J. Lin, Y.H. Yu, Y.H. Liou, Appl. Catal., B: Environ. 93 (2009) 119–125.
[25] H. Bian, Y. Wang, B. Yuan, J. Cui, X. Shu, Y. Wu, X. Zhang, S. Adeloju, New J. Chem. 37 (2013) 752–760.
[26] W.H. Lee, C.W. Lai, S.B. Abd Hamid, Materials 8 (2015) 2139–2153.
[27] D. Fang, Z. Luo, K. Huang, D.C. Lagoudas, Appl. Surf. Sci. 257 (2011) 6451–6461.
[28] H.-J. Oh, R. Hock, R. Schurr, A. Hölzing, Ch-S. Chi, J. Phys. Chem. Solids 74 (2013) 708–715.
[29] X. Zeng, Y.X. Gan, E. Clark, L. Su, J. Alloys Compd. 509 (2011) L221–L227.
[30] X. Yan, T. Ohno, K. Nishijima, R. Abe, B. Ohtani, Chem. Phys. Lett. 429 (2006) 606–610.
[31] A. Mills, Appl. Catal., B: Environ. 128 (2012) 144–149.
[32] D. Ollis, C. Gomes Silva, J. Faria, Catal. Today 240A (2015) 80–85.
[33] M.I. Litter, Appl. Catal., B: Environ. 23 (2) (1999) 89–114.
[34] M.I. Litter, Adv. Chem. Eng. 36 (2009) 37–67.
[35] M.I. Litter, N. Quici, in: B.I. Kharisov, O.V. Kharissova, H.V. Rasika Dias (Eds.), New Advances of Heterogeneous Photocatalysis for Treatment of Toxic Metals and Arsenic, John Wiley & Sons, Hoboken, 2014, pp. 145–167 Ch. 9.
[36] M.I. Litter, Pure Appl. Chem. 87 (6) (2015) 557–567.
[37] M.I. Litter, N. Quici, J.M. Meichtry, A.M. Senn, Photocatalytic removal of metallic and other inorganic pollutants, in: D.D. Dionysiou, G. Li Puma, J. Ye, J. Schneider, D. Bahnemann (Eds.), Photocatalysis: Applications, Royal Society, London, 2016, pp. 35–71, doi:http://dx.doi.org/10.1039/9781782627104-00035 Ch. 2.
[38] A. Kleiman, A. Márquez, M.L. Vera, J.M. Meichtry, M.I. Litter, Appl. Catal., B: Environ. 101 (3) (2011) 676–681.
[39] M.L. Vera, G. Leyva, M.I. Litter, J. Nanosc, Nanotech. 17 (7) (2017) 4946–4954.
[40] H.D. Traid, M.L. Vera, A.E. Ares, M.I. Litter, Mater. Chem. Phys. 191 (2017) 106–113.
[41] M.L. Vera, Preparación de fotocatalizadores de TiO_2 soportados para su uso en potabilización de aguas, Master Thesis in Materials Science and Technology, Instituto Sábato, CNEA-UNSAM, Bs.As, 2008.
[42] J.M. Meichtry, C. Colbeau-Justin, G. Custo, M.I. Litter, Appl. Catal., B: Environ. 144 (2014) 189–195.
[43] M.I. Litter, N. Quici, J.M. Meichtry, V.N. Montesinos, Photocatalytic treatment of inorganic materials with TiO_2 nanoparticles, in: H.S. Nalwa (Ed.), Encyclopedia of Nanoscience and Nanotechnology, American Scientific Publishers, Valencia, California, 2016 (in press).
[44] V.N. Montesinos, C. Salou, J.M. Meichtry, C. Colbeau-Justin, M.I. Litter, Photochem. Photobiol. Sci. 15 (2016) 228–234.
[45] J.M. Meichtry, C. Colbeau-Justin, G. Custo, M.I. Litter, Catal. Today 224 (2014) 236–243.
[46] W. Rasband, ImageJ U.S. National Institutes of Health, Bethesda, Maryland, USA, 1997–2014 ⟨http://imagej.nih.gov/ij/⟩.
[47] ASTM D1687-12. Standard Test Methods for Chromium in Water. A-Photometric Diphenyl-carbohydrazide.
[48] G.K. Mor, O.K. Varghese, M. Paulose, K. Shankar, C.A. Grimes, Sol. Energy Mater. Sol. Cells 90 (2006) 2011–2075.
[49] S. Berger, R. Hahn, P. Roy, P. Schmuki, Phys. Status Solidi B 247 (10) (2010) 2424–2435.
[50] K. Yasuda, J.M. Macak, S. Berger, A. Ghicov, P. Schmuki, J. Electrochem. Soc. 154 (9) (2007) C472–C478.
[51] M. Paulose, H.E. Prakasam, O.K. Varghese, L. Peng, K.C. Popat, G.K. Mor, T.A. Desai, C.A. Grimes, J. Phys. Chem. C 111 (2007) 14992–14997.
[52] D. Regonini, A. Satka, D.W.E. Allsopp, A. Jaroenworaluck, R. Stevens, C.R. Bowen, J. Nanosci. Nanotech. 9 (2009) 4410–4416.
[53] S. So, K. Lee, P. Schmuki, J. Am. Chem. Soc. 134 (2012) 11316–11318.
[54] A.B. Murphy, Sol. Energy Mater. Sol. Cells 91 (14) (2007) 1326–1337.
[55] Y. Mizukoshi, N. Ohtsu, S. Semboshi, N. Masahashi, Appl. Catal., B: Environ. 91 (1) (2009) 152–156.
[56] Y.-H. Chang, Ch-M. Liu, H.-E. Cheng, Ch. Chen, ACS Appl. Mater. Interfaces 5 (2013) 3549–3555.
[57] O.K. Varghese, D. Gong, M. Paulose, C.G. Grimes, E.C. Dickey, J. Mater. Res. 18 (2003) 156–165.
[58] Y. Lai, L. Sun, Y. Chen, H. Zhuang, Ch. Lin, J.W. Chin, J. Electrochem. Soc. 153 (7) (2006) D123–D127.
[59] J. Criado, C. Real, Faraday Trans. 179 (12) (1983) 2765–2771.
[60] D.J. Reidy, J.D. Holmes, M.A. Morris, J. Eur. Ceram. Soc. 26 (2006) 1527–1534.
[61] D.A.H. Hanaor, Ch.C. Sorrell, J. Mater. Sci. 46 (2011) 855–874.
[62] Y.R. Smith, A. Kar, V. Subramanian, Ind. Eng. Chem. Res. 48 (2009) 10268–10276.
[63] A. Mazzarolo, K. Lee, A. Vicenzo, P. Schmuki, Electrochem. Commun. 22 (2012) 162–165.